Time of Flight Transmission Mode Ultrasound Computed Tomography With Expected Gradient and Boundary Optimization

Roberto C. Ceccato, Andre V. Pigatto, Richard C. Aster, Chi-Nan Pai, Jennifer L. Mueller, *Senior Member, IEEE*, and Sérgio S. Furuie

Abstract*—*Objective: **Quantitative time of flight in transmission mode ultrasound computed tomography (TFTM USCT) is a promising, cost-effective, and non-invasive modality, particularly suited for functional imaging. However, TFTM USCT encounters resolution challenges due to path information concentration in specific medium regions and uncertainty in transducer positioning. This study proposes a method to enhance resolution and robustness, focusing on low-frequency TFTM USCT for pulmonary imaging.** ***Methods:*** **The proposed technique improves the orientation of steepest descent algorithm steps, preventing resolution degradation due to path information concentration, while allowing for *a posteriori* sensor positioning retrieval. Total variation regularization is employed to stabilize the inverse problem, and a modified Barzilai-Borwein method determined the step size in the steepest descent algorithm. The proposed method was validated through simulations of data on healthy and abnormal cross-sections of a human chest using MATLAB's k-Wave toolbox. Additionally, experimental data were collected using a Verasonics Vantage 64 low-frequency system and a ballistic gel torso-mimicking phantom to assess robustness under a more realistic environment, closer to that of a clinical situation.** ***Results:*** **The results showed that the proposed method significantly improved image quality and successfully retrieved sensor locations from imprecise positioning.** ***Significance:*** **This study is the first to address transducer location uncertainty on a transducer belt in TFTM USCT and to apply an estimated gradient approach. Additionally, low-frequency USCT for lung imaging is quite novel, and this work addresses practical questions that will be important for translational development.**

***Index Terms*—Ultrasound computed tomography, boundary optimization, time of flight transmission mode.**

Received 19 July 2024; revised 2 November 2024, 14 January 2025, and 12 February 2025; accepted 3 March 2025. Date of publication 12 March 2025; date of current version 22 August 2025. The work of Roberto C. Ceccato was supported by São Paulo Founding Agency FAPESP under Grant 2021/13997-0 and Grant 2023/15074-1. This work was supported by the National Institute of Biomedical Imaging and Bioengineering of the National Institutes of Health under Award R21EB024683. *(Corresponding author: Roberto C. Ceccato.)*

Roberto C. Ceccato is with the Polytechnic School, University of São Paulo São Paulo 05508-010, Brazil (e-mail: roberto.ceccato@usp.br).

Sérgio S. Furuie is with the Polytechnic School, University of São Paulo, Brazil.

Andre V. Pigatto was with the School of Biomedical Engineering, Colorado State University, USA.

Richard C. Aster is with Geosciences Department, Colorado State University, USA.

Chi-Nan Pai is with the Polytechnic School, University of São Paulo, Brazil.

Jennifer L. Mueller is with the Department of Mathematics and School of Biomedical Engineering, Colorado State University, USA.

Digital Object Identifier 10.1109/TBME.2025.3550823

I. Introduction

ULTRASOUND (US) imaging is a safe, portable and cost-effective method widely used by clinicians to diagnose and identify early disease symptoms. The most common form of ultrasonic imaging, B-mode, produces anatomical grayscale images with each pixel proportional to the amplitude of the logarithmically compressed envelope of the echoes produced by the interrogated tissues from excitation pulses [2]. B-mode ultrasound is currently used as a supplemental modality in breast cancer screening when an abnormality is identified on a mammogram or in evaluating a symptomatic breast. The American College of Radiology recommends this imaging modality as the preferred choice for women under 30, as well as for pregnant or lactating women. It is also advised as a supplemental screening tool for detecting occult breast cancer when MRI is unavailable or contraindicated.

As a promising alternative, ultrasound computed tomography (USCT) has several advantages over B-mode imaging. The quantitative tomographic images are easy to interpret and provide information on the physical properties of the tissue in each pixel. Also, it is not subject to the ultrasound technician's operating skill, and provides a more spatially accurate anatomical image. For breast cancer detection, the commercial USCT Softvue system has been FDA approved for dense breast cancer screening as an adjunct to mammography [3]. Such systems make use of a ring transducer in a water-filled chamber with the subject lying prone on a table and the breast suspended in the water. Speed of sound (SoS), reflection, and attenuation are reconstructed from data collected on many transducers (typically over 2000) in the MHz range. Conventional US has also been studied as a thoracic bedside technology for diagnosis and monitoring [4], but due to the lack of signal penetration into lung tissue, US images often contain more of their information in artifacts than in the images themselves [5].

In [6] it was shown that sound waves are efficiently transmitted through the thorax for frequencies between 10 and 750 kHz, with signal attenuation increasing as frequency increases. Rueter et al. [6] found that transmission during expiration was significantly decreased in patients suffering from pulmonary emphysema or pneumothorax, but increased in patients with pleural effusions. Morenz et al. [7] demonstrated US waves transmitted at 1–40 kHz propagate through human lung tissue in patients with COPD, and differences in the high pass frequency between inspiratory and expiratory signals can be seen for patients in diseased states. While the studies [6], [7] did not include tomographic reconstructions, the work inspired further research in low-frequency (LF) USCT for lung imaging [8], [9].

The main quantitative USCT methods include Full Waveform Inversion (FWI) [10], [11], [12], elastography [13], time of flight in echo mode (TFEM) [14], [15], [16], and time of flight in transmission mode (TFTM) [17], [18]. TFTM USCT reconstructs the speed of sound distribution within the region of interest by analyzing the travel path and time of flight of ultrasound pulses. Transducers are distributed around the perimeter of the domain, and the time of flight from the pulsed wavefront first arrival, traveling from one transmitter through the medium to all other transducers acting as receivers, is used to characterize the interior (without accounting for reflections).

However, for the application of bedside lung imaging, an additional challenge arises. In contrast to breast imaging, the region of interest cannot be suspended in a tank of water surrounded by a rigid transducer ring. Instead, the transducers are in contact with the body, arranged circumferentially around the torso on a flexible belt. This inevitably results in uncertainties in transducer location. In [8] LF USCT data was collected on a belt of 28 transducers placed around a phantom human torso constructed of ballistic gel. As a fast or real-time reconstruction algorithm is required for dynamic bedside lung imaging, TFTM USCT was the quantitative method of choice.

In addition to sensor positioning imprecision, TFTM USCT faces challenges due to its reliance on the first arrival of the wavefront and ray-path theory [18], [19]. Some pixels in the discretized domain receive far more path information than others, leading to solutions trapped in local minima with high local contrasts. To address these issues without compromising portability or requiring complex hardware, this work proposes two key improvements to the standard TFTM USCT methods [17], [18]. First, the steepest descent algorithm steps are calculated using an expected value for the gradient, reducing path information discrepancies throughout the pixels, decrasing the level of regularization and enhancing spatial resolution with physical meaningful solutions. Second, *a posteriori* boundary optimization based on normal directional offsets and estimated boundary SoS is introduced to improve the sensor location accuracy during the reconstruction.

To study the sensitivity of the algorithm to errors in transducer locations, numerical simulations of a simplified 2-D cross section from the human chest with two different lung injuries and sensor positioning perturbations were conducted using the MATLAB toolbox k-Wave [20]. These simulations allowed for quantitative evaluation and demonstrated how the proposed method improves resolution and reconstructed sound speed accuracy compared to the standard TFTM method. Additionally, experimental data were collected using a Verasonics Vantage 64 low-frequency system, 28 Tonpilz-type transducers arranged in a belt, and a ballistic gel torso-mimicking phantom. The reconstructions from simulated and experimental datasets showed improvements in image resolution, both quantitatively and qualitatively. In numerical simulations with known ground-truth sensor positions, the method retrieved the positions within 2 mm root mean square error accuracy. This is the first work to address the problem of uncertainty in transducer location on a transducer belt, and the first to use the estimated gradient approach in TFTM USCT. The application of LF USCT for lung imaging is also novel, and this work addresses key practical questions for translational development.

This paper is organized as follows, Section II-A presents the theoretical background for TFTM USCT. The proposed method theory and demonstration are detailed in Section II-B for the expected gradient steepest descent step size determination and Section II-C for the *a posteriori* sensor positioning and boundary optimization. Sections III-A and III-B describe the materials and methods used for *in silico* simulations and *ex vivo* experimental reconstructions, respectively. A brief overview of the chosen algorithms is provided in the Section III-C. The results and discussions for both simulated and experimental data are presented in Sections IV-A and IV-B. Finally, the conclusions are presented.

II. Theory

A. TFTM USCT Background

TFTM USCT is based on the relationship between the ultrasound pulse wavefront first arrival time delay between transmitter and the receiver, its traveled path, and the slowness distribution over a medium Ω. Let $\sigma(r)$ denote the slowness distribution of the medium in a position r, which is the inverse of the SoS, H the system that models the paths from transmitters to receivers, and t the observed time delay estimated data.

Typically to solve the inverse problem of determining σ from measured data t, one would have to approximate the forward problem H. The straightforward alternative is to solve the general wave equation on the given domain while recording the time of flight (ToF) and the path between transmitter and receiver. The pressure $p(r;t)$ satisfies the wave equation with point source $g(r;t)$,

$$\nabla^2 p(r;t) - \frac{1}{c(r)^2}\frac{\partial^2}{\partial t^2} p(r;t) = g(r;t). \tag{1}$$

Here, for a general position r, $c(r) = \lambda(r) f$ represents the local SoS, $\lambda(r)$ is the local wavelength, and f the source central frequency.

Nevertheless, solving the aforementioned partial differential equation is an extremely expensive computational task. If one assumes a time-harmonic solution, such as,

$$p(r;t) = A(r)\exp^{j\omega(t-T(r))} \tag{2}$$

where $A(r)$ is the amplitude of the ultrasound pulse in position r, ω is the central angular frequency, $T(r)$ is the front wave first arrival time delay between the transmitter and the receiver, and j is the imaginary unit, the wave equation can be expanded to

$$\left(\frac{\nabla^2 A}{\omega^2 A} - \frac{2j\nabla A \cdot \nabla T}{\omega A} + \frac{jA\nabla^2 T}{\omega A}\right) + \left(\frac{1}{c(r)^2} - \nabla T \cdot \nabla T\right) = 0. \tag{3}$$

The first parenthetical part of (3) is called the Transport Equation and the second one the Eikonal Equation [19]. For ray-theory conditions – frequency considerably greater than the wavefront amplitude and its first and second derivative [21] – the two partial differential equations can be uncoupled by assuming that the Transport Equation tends to zero. This results in the Eikonal Equation,

$$\| \nabla T(r) \|_2^2 = \frac{1}{c(r)^2} = \sigma(r)^2. \tag{4}$$

Let $\Omega \subseteq \mathbb{R}^3$ denote the spatial domain of interest, where the Eikonal Equation is formulated as an initial value problem [22]. The time delay phase field is represented by the mapping $T : \Omega \to \mathbb{R}$, satisfying the following conditions

$$\begin{cases} \| \nabla T(r) \|_2^2 = \frac{1}{c(r)^2}, & r \in \Omega \\ T(r) = T_0(r) & r \in \Gamma \subseteq \Omega \end{cases} \tag{5}$$

where Γ specifies the initial boundary with known wavefront shape, and $T_0 : \Gamma \to \mathbb{R}$ provides its initial condition values. Typically, Γ is considered a point source with $T_0 = 0$ within the TFTM USCT field. For this study, it is assumed that all ray-paths converge at the center of the transducer element, irrespective of the transducer size. Consequently, the time delay map value evaluated at position r from a source in r_i is denoted as $T_{r_i}(r)$.

Compared to other wavefront path-solver methods, the Eikonal equation can be solved more efficiently using fast marching methods (FMM) [22], [23], [24]. These methods provide a sufficiently accurate approximation of the first arrival of the wavefront at receiver positions. Once the forward problem $T_{r_i}(r)$ is resolved for a transmitter at r_i, the wavefront first arrival path can be estimated for each receiver. This path may be a straight line or a refraction-corrected path, obtained by applying Fermat's principle and utilizing a gradient descent method starting from the location of the receivers [17], [18]. In this work, all paths are computed considering sound wave refraction to enhance accuracy. Consequently, the observed ToF between a transmitter and a receiver located at a general position r_j is represented by the path integral of the slowness along the wavefront first arrival path L_{r_i,r_j} as follows

$$T_{r_i}(r_j) = \int_{L_{r_i,r_j}} \sigma(l)dl. \tag{6}$$

Assume that all valid observed times of flight, i.e., data with its expected measurement errors within a desired limit, are stored in a vector $\mathbf{t}$. A general entry q corresponds to its respective numerically calculated ToF as $\mathbf{t}_q = T_{r_i}(r_j) + \varepsilon_q$, where ε_q represents the modeling and measurement error in the ToF estimation. This leads to

$$\mathbf{t}_q = \int_{L_{r_i,r_j}} \sigma(l)dl + \varepsilon_q. \tag{7}$$

By approximating the measured and numerically calculated times of flight while neglecting the measurement and modeling errors ε, one can leverage the linearity of (7) and discretize it in a vector form to solve the inverse problem computationally. After discretizing the entire domain Ω into n pixels, the path-length traveled by the wavefront per discrete element is stored in each entry of a column vector $\mathbf{h} \in \mathbb{R}^n$. The slowness distribution is represented by a vector $\boldsymbol{\sigma} \in \mathbb{R}^n$, containing pixel-wise approximations of the property. This yields the following vector-form approximation of (7)

$$\mathbf{h}_q' \boldsymbol{\sigma} = \mathbf{t}_q. \tag{8}$$

Therefore, by stacking the transposed path vector and all valid ToF combinations between transmitters and receivers, one obtains the matrix form

$$\mathbf{H}\boldsymbol{\sigma} = \mathbf{t}. \tag{9}$$

Here, $\mathbf{H} \in \mathbb{R}^{m \times n}$ represents the ray-path matrix [25] that discretizes the space into n pixels or voxels and accumulates the path length within each pixel or voxel associated with each of the m reliable ToF measurements. The vector $\boldsymbol{\sigma} \in \mathbb{R}^n$ stores the slowness for each pixel or voxel, and $\mathbf{t} \in \mathbb{R}^m$ denotes the m measurements of ToF. In Fig. 2, the general formation of the i-th row of the matrix $\mathbf{H}$, originating from a transmitter located at r_i, is depicted under the straight-line approximation of the wavefront path while assuming the validity of all observations. It is evident that pixels closer to the transmitter will encapsulate a significantly greater amount of path information per pixel. In

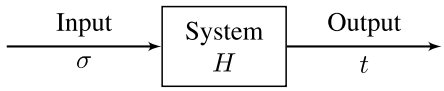

Fig. 1. Inverse problem equation and scheme representation.

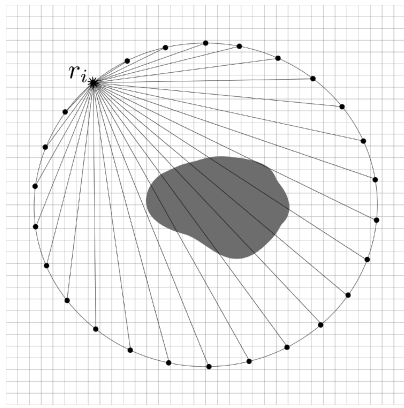

Fig. 2. Illustrative depiction of the paths contributing to the i-th row of the $\mathbf{H}$ matrix. The image highlights the significantly greater path information captured by pixels closer to the transmitter at position r_i compared to those situated further within the domain.

contrast, pixels situated at greater distances within the domain may contribute minimally or lack any path information, thereby having negligible influence on the matrix formation.

It is important to note that a solution $\boldsymbol{\sigma}$ precisely satisfying (9) is generally unattainable because $\mathbf{t}$ generally does not belong to the range of $\mathbf{H}$. This is mainly due to the system being underdetermined, as certain pixels lack information because they are not intersected by any ray paths. Therefore, the objective is to find the best approximation of the input vector that minimizes the discrepancy between the measured and achievable output data vectors. This can be accomplished through least-squares optimization by reformulating the problem as

$$\arg\min_{\boldsymbol{\sigma}} J(\boldsymbol{\sigma}) = \| \mathbf{H}\boldsymbol{\sigma} - \mathbf{t} \|_2^2 . \tag{10}$$

The inverse problem associated with the forward problem presented by (9) is well known to be ill-posed [26], [27], and the matrix $\mathbf{H}$ is typically severely ill-conditioned [27], [28]. Consequently, it is not advisable to solve the optimization problem stated in (10) with elementary minimization methods or matrix inversions [18], [27]. The cost function should be regularized with a function $G(\boldsymbol{\sigma})$ weighted by a α factor as follows

$$\arg\min_{\boldsymbol{\sigma}} J(\boldsymbol{\sigma}) = \| \mathbf{H}\boldsymbol{\sigma} - \mathbf{t} \|_2^2 + \alpha G(\boldsymbol{\sigma}). \tag{11}$$

The function $G(\boldsymbol{\sigma})$ is usually either a Tikhonov or Total Variation regularization function within the field of quantitative ultrasound imaging reconstruction [17], [18], [29], [30]. To solve this type of nonlinear optimization effectively and robustly, the steepest gradient method is a well-established approach [26], [31], [32].

B. The Expected Gradient

The general solution method for (11) uses an initial guess for the SoS to approximate the forward problem and then solve the inverse problem with any desired steepest gradient stopping criteria. The steepest gradient solution is used to update the forward problem approximation and try to avoid local minima. This process of solving and updating is repeated until an overall desired stopping criteria is achieved. A more precise general description of it can be found in [18], but the main steps are

1) Approximate the forward problem using the Eikonal equation and determine the wavefront first arrival path with an initial SoS conjecture.
2) Solve (11) using a steepest descent algorithm until a desired stopping criteria is achieved (e.g. number of iterations, or relative residual error).
3) Use the solution from step 2 as a new SoS conjecture in order to re-approximate the forward problem system.
4) Repeat step 2 with the new approximation.
5) Repeat steps 3 and 4 until a global stopping criteria is achieved (e.g. number of forward problem updates, or relative residual error).

Now, assume a general l-th forward problem update, which is not referenced in the following derivation equations for the sake of notation simplicity. If one takes the main component of the cost function in the k-th iteration of the gradient descent algorithm,

$$J\left(\boldsymbol{\sigma}^k\right) = \| \mathbf{H}\boldsymbol{\sigma}^k - \mathbf{t} \|_2^2 + \alpha G\left(\boldsymbol{\sigma}^k\right), \tag{12}$$

the cost function gradient with respect to the slowness is given by

$$\nabla_{\boldsymbol{\sigma}^k} J\left(\boldsymbol{\sigma}^k\right) = 2\left(\mathbf{H}'\mathbf{H}\boldsymbol{\sigma}^k - \mathbf{H}'\mathbf{t}\right) + \alpha \nabla_{\boldsymbol{\sigma}^k} G\left(\boldsymbol{\sigma}^k\right) \tag{13}$$

where $\mathbf{H}'$ is the transpose of $\mathbf{H}$. Thus, its steepest gradient update with a β_k step size should be

$$\boldsymbol{\sigma}^{k+1} = \boldsymbol{\sigma}^k - \beta_k \left(2\left(\mathbf{H}'\mathbf{H}\boldsymbol{\sigma}^k - \mathbf{H}'\mathbf{t}\right) + \alpha \nabla_{\boldsymbol{\sigma}^k} G\left(\boldsymbol{\sigma}^k\right)\right). \tag{14}$$

Let us define $\delta\mathbf{t}^k = \mathbf{H}\boldsymbol{\sigma}^k - \mathbf{t}$ and $\mathbf{q}^k = 2(\mathbf{H}'\mathbf{H}\boldsymbol{\sigma}^k - \mathbf{H}'\mathbf{t})$, so that,

$$\mathbf{q}^k = 2\mathbf{H}'\delta\mathbf{t}^k. \tag{15}$$

Therefore, for a total of m valid time delay estimations, the j-th entry of $\mathbf{q}^k$ will be given by

$$\mathbf{q}_j^k = 2\sum_{i=1}^{m} \mathbf{H}'_{j,i}\delta\mathbf{t}_i^k = 2\sum_{i=1}^{m} \mathbf{H}_{i,j}\delta\mathbf{t}_i^k. \tag{16}$$

If one replaces (15) in (14)

$$\boldsymbol{\sigma}^{k+1} = \boldsymbol{\sigma}^k - \beta^k \nabla_{\boldsymbol{\sigma}^k} J\left(\boldsymbol{\sigma}^k\right) \tag{17}$$

$$= \boldsymbol{\sigma}^k - \beta^k \left(\mathbf{q}^k + \alpha \nabla_{\boldsymbol{\sigma}^k} G\left(\boldsymbol{\sigma}^k\right)\right). \tag{18}$$

It then becomes evident that each entry $\mathbf{q}_j^k$ arises from the product of different columns of the matrix $\mathbf{H}$ with the same $\delta\mathbf{t}_i^k$ values. Consequently, variations in these entries from $\mathbf{q}^k$ are attributable to differences in the construction of the matrix $\mathbf{H}$. Hence, the solution to the problem, as expressed in (14), emphasizes updates on pixels that contain more path information. This is due to the fact that columns of the matrix $\mathbf{H}$ with a greater number of nonzero elements will yield larger multiplication results with the $\delta\mathbf{t}_i^k$ vector, as all entries of the matrix and vector are non-negative. Pixels in proximity to the transducers are likely to intersect more paths since all paths originate from and terminate at a transducer, thereby contributing more substantially to the overall path information. Conversely, some pixels situated away from the domain boundary may lack any intersecting paths. This phenomenon is illustrated in the Fig. 2 from the previous subsection. Essentially, the straightforward computation of the Jacobian results in updates that disproportionately affect certain positions. Consequently, the gradient descent step applies with greater intensity at these positions, potentially leading to local minima that do not necessarily reflect reality or maintain consistent physical significance.

The suggestion proposed here to overcome this matter is to get a general expected path-per-pixel value considering every observation by calculating a expected gradient in each update. This would be given by

$$\boldsymbol{\sigma}^{k+1} = \boldsymbol{\sigma}^k - \beta^k \mathbb{E}\left[\nabla_{\boldsymbol{\sigma}^k} J\left(\boldsymbol{\sigma}^k\right)\right]$$

$$= \boldsymbol{\sigma}^k - \beta^k \left(\mathbb{E}\left[\mathbf{q}^k\right] + \mathbb{E}\left[\alpha \nabla_{\boldsymbol{\sigma}^k} G\left(\boldsymbol{\sigma}^k\right)\right]\right). \tag{19}$$

Here $\mathbb{E}[\mathbf{q}^k]$ is approximated as follows for the sake of simplicity

$$\mathbb{E}\left[\mathbf{q}_j^k\right] \approx \frac{1}{1+w_j} 2 \sum_{i=1}^{m} \mathbf{H}'_{j,i} \delta \mathbf{t}_i^k \tag{20}$$

where w_j is the number of nonzero elements in the j-th column of matrix $\mathbf{H}$. Also, as the regularization function term is independent of the number of observations per pixels

$$\mathbb{E}\left[\alpha \nabla_{\boldsymbol{\sigma}^k} G(\boldsymbol{\sigma}^k)\right] = \alpha \nabla_{\boldsymbol{\sigma}^k} G\left(\boldsymbol{\sigma}^k\right) \tag{21}$$

Therefore, the steepest descent algorithm update procedure proposed in this work is the following for any slowness vector entry

$$\boldsymbol{\sigma}_j^{k+1} = \boldsymbol{\sigma}_j^k - \beta^k \left(\frac{1}{1+w_j} 2 \sum_{i=1}^{m} \mathbf{H}'_{j,i} \delta \mathbf{t}_i^k + \alpha \nabla_{\boldsymbol{\sigma}^k} G(\boldsymbol{\sigma}^k)_j \right). \tag{22}$$

C. Boundary Optimization

A notable problem in TFTM USCT imaging is the imprecision regarding transducers positioning. Along with inherit measurement error there is an uncertainty associated with basal movements, such as chest expansion and relaxation. To overcome this issue, it is proposed to optimize the transducer positions *a posteriori*, starting from the best possible estimate, as a new cost function for every l-th forward problem update. This concept is based on the static correction term used in seismic tomographic imaging to correct for Earth properties near the surface [33], [34]. This method tries to best fit the forward model to the observed ToF by adding a sensor-specific correction term. For the TFTM USCT problem, this would have the following format

$$\mathbf{H}^l \boldsymbol{\sigma}^{l,k} + \boldsymbol{\xi}^l \approx \mathbf{t} \tag{23}$$

where $\boldsymbol{\xi}^l \in \mathbb{R}^m$ is the correction term for each observation after the SoS optimization in the l-th forward problem update.

To establish the relationship between the correction term $\boldsymbol{\xi}^l$ and the displacement of the sensors in (23), one shall assume a known slowness $\tilde{\sigma}|_{\partial\Omega}$ at the boundary $\partial\Omega$ of the domain and postulate that the initial arrival ray-paths intersect the sensor surface perpendicularly. Additionally, assuming approximately uniform lateral displacement due to the equal transducer spacing in the belt, sensor position errors can be constrained to the normal direction. Consequently, displacement in this direction can be related to the temporal correction term using the estimated speed of sound at the boundary, effectively reducing the problem to one degree of freedom per transducer. This relationship can be expressed in matrix form as follows

$$\mathbf{H}^l \boldsymbol{\sigma}^{l,k} + \boldsymbol{\xi}^l = \mathbf{H}^l \sigma^{l,k} + \mathbf{C} \Delta \mathbf{r}^l \approx \mathbf{t}. \tag{24}$$

Let $\Delta \mathbf{r}^l \in \mathbb{R}^{n_s}$ represent the array of displacements in the normal direction for each of the n_s sensors. Then, the matrix $\mathbf{C} \in \mathbb{R}^{m \times n_s}$ is structured such that each row has non-zero entries equal to the prior boundary slowness $\tilde{\sigma}|_{\partial\Omega}$ only at the entries corresponding to the transmitter and receiver associated with the same row in the matrix $\mathbf{H}$. For example, consider the i-th row of $\mathbf{H}$, which relates to a specific transmitter-receiver pair (tx, rx). The i-th row of $\mathbf{C}$ is then defined accordingly

$$\mathbf{C}_{i,j} = \begin{cases} \tilde{\sigma}|_{\partial\Omega}, & \text{if } j = \{tx, rx\} \\ 0, & \text{otherwise.} \end{cases} \quad \forall j = \{1, \ldots, n_s\} \tag{25}$$

Moreover, to maintain the integrity of the boundary shape, regularization with a smoothing operator is applied to the displacement array optimization. This approach is essential because the boundary optimization problem is highly overdetermined, since there are many more ToF observations than sensors, and abrupt changes in the boundary topology are undesirable and unrealistic due to tension on the belt. Therefore, changes in the boundary should remain locally smooth relative to the positions of the transducers. Although constrained L^1 norm regularizations are typically recommended for overdetermined problems [35], this particular problem is formulated using Tikhonov regularization with a second-order first derivative operator, since a damped result is preferred over an edge-sharpening one. The Tikhonov regularization serves as a direct method to address a Morozov and Ivanov multi-objective optimization [36], [37], [38], streamlining computational processes. In this context, the Morozov regularization enforces the second-order first derivative of the displacement array to be zero, while incorporating the optimization of sensor positioning as constraints. The Laplacian differential regularization operator is henceforth denoted by the matrix $\mathbf{D}$, constructed as follows

$$\mathbf{D}_{i,j} = \begin{cases} -2, & \text{if } j = \{i\} \\ 1, & \text{if } j = \{i-1, i+1\} \\ 0, & \text{otherwise.} \end{cases} \quad \forall i = \{1, \ldots, n_s\} \tag{26}$$

Therefore, the reconstruction problem now comprises two cost functions states as

$$\begin{aligned} \arg\min_{\boldsymbol{\sigma}^{l,k}} J\left(\boldsymbol{\sigma}^{l,k}\right) &= \| \mathbf{H}^l \boldsymbol{\sigma}^{l,k} - \mathbf{t} \|_2^2 + \alpha_1 G\left(\boldsymbol{\sigma}^{l,k}\right) \\ \arg\min_{\Delta \mathbf{r}^l} F\left(\boldsymbol{\sigma}^{l,k}, \Delta \mathbf{r}^l\right) &= \| \mathbf{C} \Delta \mathbf{r}^l + \left(\mathbf{H}^l \boldsymbol{\sigma}^{l,k} - \mathbf{t}\right) \|_2^2 \\ &\quad + \alpha_2 \| \mathbf{D} \Delta \mathbf{r}^l \|_2^2 \end{aligned} \tag{27}$$

where α_1 and α_2 are the respective regularization weighting factors. The minimization process of the first cost function was previously explained in Sections II-A and II-B. Now, for the second cost function $F(\boldsymbol{\sigma}^{l,k}, \Delta \mathbf{r}^l)$, it is easy to see that its parts can be stacked in order to gather everything in one single least squares problem,

$$\begin{aligned} F\left(\boldsymbol{\sigma}^{l,k}, \Delta \mathbf{r}^l\right) &= \| \mathbf{C} \Delta r^l + \left(\mathbf{H}^l \boldsymbol{\sigma}^{l,k} - \mathbf{t}\right) \|_2^2 + \alpha_2 \| \mathbf{D} \Delta \mathbf{r}^l \|_2^2 \\ &= \left\| \begin{bmatrix} \mathbf{C} \\ \alpha_2^2 \mathbf{D} \end{bmatrix} \Delta \mathbf{r}^l + \begin{bmatrix} \left(\mathbf{H}^l \boldsymbol{\sigma}^{l,k} - \mathbf{t}\right) \\ \mathbf{0} \end{bmatrix} \right\|_2^2. \end{aligned} \tag{28}$$

TABLE I
SUMMARY OF THE NUMERICAL PHANTOM CHARACTERISTICS

	Background	Torso	Lungs	Pathology	Spine and Ribs	Heart
Speed of Sound $[m/s]$	1500	1540	1400	1580	1900	1560
Density $[kg/m^3]$	1000	1000	900	1080	1200	1080
Attenuation $[Np/(m \cdot MHz^{1.1})]$	0.022	7	160	7	45	3

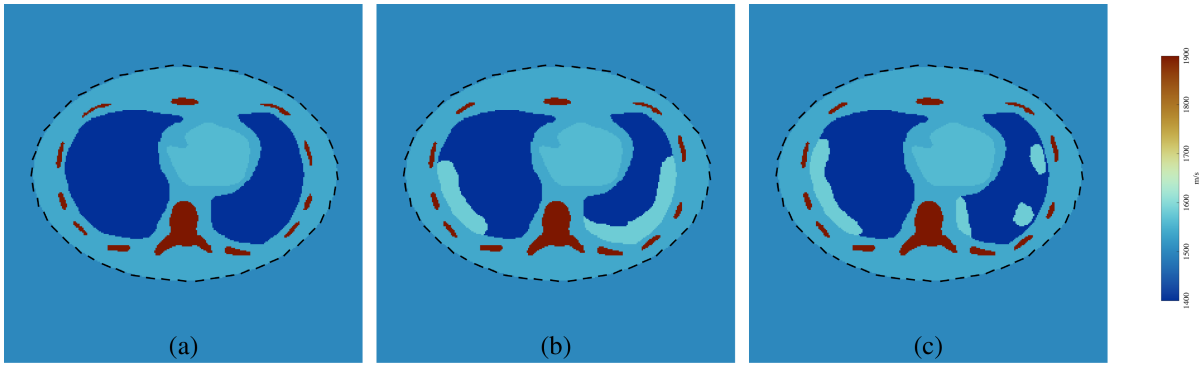

Fig. 3. Speed of sound distribution of the simplified human chest cross-section phantom reference (a), with bilateral edema (b), and multiple collection of fluids in both lungs (c).

The Moore-Penrose pseudo inverse solution for the cost function $F(\boldsymbol{\sigma}^{l,k}, \Delta\mathbf{r}^l)$ is defined as follows

$$\Delta\mathbf{r}^l = \left(\begin{bmatrix} \mathbf{C} \\ \alpha_2^2\mathbf{D} \end{bmatrix}' \begin{bmatrix} \mathbf{C} \\ \alpha_2^2\mathbf{D} \end{bmatrix} \right)^{-1} \begin{bmatrix} \mathbf{C} \\ \alpha_2^2\mathbf{D} \end{bmatrix}' \begin{bmatrix} (\mathbf{H}^l\boldsymbol{\sigma}^{l,k} - \mathbf{t}) \\ \mathbf{0} \end{bmatrix} \tag{29}$$

Therefore, the proposed solution method for the inverse problem with boundary optimization is

1) Initialize the slowness distributions values for the medium and boundary.
2) Estimate the forward problem by running the Fast Marching Method (FMM) and thus generate matrix $\mathbf{H}^l$.
3) Solve the optimization over the $J(\boldsymbol{\sigma}^{l,k})$ cost function until a desired stopping criteria is achieved (e.g. number of iterations, or relative residual error).
4) Solve the optimization problem regarding the $F(\boldsymbol{\sigma}^{l,k}, \Delta\mathbf{r}^l)$ cost function with the Moore-Penrose Pseudo inverse.
5) Use the calculated displacement to update the sensor positions' coordinates. This procedure will apply the displacement changes directly in the execution of the forward problem.
6) End if a global stopping criteria is achieved, otherwise return to step 2.

The adjustment of the sensor position may be interpreted as a modification within the solution space, resulting from alterations in the $\mathbf{H}^{l,k}$ matrix, to minimize the residual of the $J(\boldsymbol{\sigma}^{l,k})$ cost function. Rather than solely adjusting the solution space of $\mathbf{H}^{l,k}$ through path updates with refraction corrections, the relocation of the sensor introduces an additional degree of freedom. This facilitates a more precise alignment of the solution while ensuring the preservation of physical significance and hence reducing the cost function residual. Along with the expected gradient method, the boundary optimization is part of the complete solution method used to compute the results in this paper.

III. MATERIALS AND METHODS

A. Numerical Simulations

To validate the proposed method, one reference and two distinct abnormal numerical phantoms were generated and simulations executed using the k-Wave toolbox for MATLAB [20], [39]. Consistent with previous group studies and the primary objective of respiratory activity monitoring [8], [30], [40], each phantom represents a simplified DICOM oriented cross-section of the human thorax. The reference phantom representing a healthy subject, is shown in Fig. 3(a). Abnormal numerical phantoms, shown in Fig. 3(b), and 3(c), include regions designed to simulate high-density, viscous purulent areas commonly found in ground-glass opacities in early-stage COVID-19 patients. The assumed acoustic properties of the anatomical structures are detailed in Table I [41], [42]. The SoS value for the spine was selected to represent the average of its trabecular bone composition: red marrow (lower SoS) and a thin outer layer of compact bone (higher SoS). The same SoS was assigned to the ribs, as they consist of flat bone with a similar structure.

The simulation domain was defined as a rectangular prism of $400 \times 400 \times 22.5\,\text{mm}^3$ discretized into $251 \times 251 \times 16$ pixels. The third dimension was introduced solely to account for the transducer width. The time sampling period was 6.67 μs. For the transducer belt modeling, 52 elements with 10 mm width were evenly distributed along an ellipse with minor and major axes of 240 mm and 340 mm, respectively. The transducer elements are depicted to scale as black lines in in Fig. 3(a)–(c). Given the aim to reconstruct a domain analogous to the human torso, a low center frequency of 150 kHz was selected, based on [6]. A

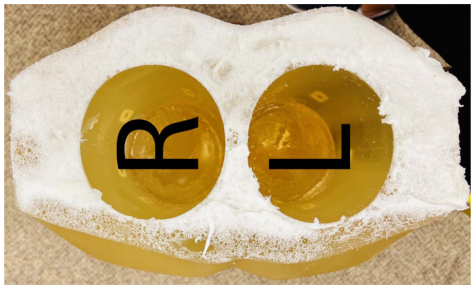

Fig. 4. Top view of the torso phantom. Posterior (back) at the top of image, anterior (chest) at the bottom. Right and left cavities are labeled R and L.

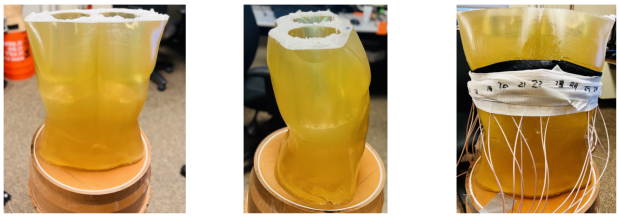

(a) (b) (c)

Fig. 5. Body-torso phantom anterior view (a), right-lateral view (b) and anterior view with the transducers belt (c).

Gaussian envelope with three cycles was used as the transmitted pulse morphology. Acquisition noise was simulated by adding normally distributed noise with a standard deviation equal to 5% of the average dynamic range of all received amplitudes.

B. Experimental Torso-Shaped Phantom

Besides *in silico* data validation, reconstructions were computed using *ex vivo* experimental data. This methodology aimed to reveal the method's performance under conditions that more closely resemble clinical settings and applications. For this purpose, a torso-shaped phantom was constructed by filling a standard mannequin with ballistic gel. The ballistic gel was prepared according to a target volume (V_t) recipe, consisting of $0.216V_t$ grams of gelatin, $0.3V_t$ liters of glycerin, and $0.9V_t$ liters of saline with 0.042% concentration. The resulting phantom exhibited an average SoS of 1870 m/s. To simulate lung structures, two 110 mm diameter cylinders were immersed in the gel during the curing process and later removed. The resulting cavities can be seen in Fig. 4. More views of the experimental setup and phantom are provided in Fig. 5. Regarding ultrasound transmission and acquisition, 28 Tonpilz-type transducers, each with a center frequency of 125 kHz, were attached to the inframammary fold line using a belt, as illustrated in Fig. 5(c). An initial estimate of the boundary and sensor positions was obtained with an Artec^{TM} 3-D scanner. These transducers were interfaced with a Verasonics Vantage 64 Low-Frequency Research Ultrasound System for electrical signal excitation and reception. During each transmission cycle, one transducer emitted a pulse modulated by a Gaussian envelope comprising 2.5 cycles, while the remaining 27 transducers served as receivers for the wavefront propagating through the medium. The received analog signals were filtered and sampled by the Verasonics Vantage System, followed by a post-processing in MATLAB.

The post-processing procedure encompasses the following main steps. Initially, signal calibration based on a sensitivity coefficient experimentally identified for each transmitter-receiver pair is conducted. Subsequently, the DC component and voltage drift are eliminated using a moving average subtraction method. The third step involves windowing the signal, with the start positioning settled to the first arrival instant calculated by threshold detection. The window duration is set to match the duration of the transmitted pulse. Finally, the signal undergoes filtering using a 12-th order low–pass Butterworth filter, with a cutoff frequency equal to 175 kHz. More details on hardware, experimental setup, data acquisition, and post-processing are available in [8], [9].

C. The Speed of Sound Reconstruction

Once in possession of the simulated or experimental radio-frequency ultrasound signal (rf-US), the ToF has to be calculated. For computer-simulated data, the ToF estimation was conducted using a normalized cross-correlation (NCC) maximum search method. To minimize the influence of spurious data, a threshold of 0.65 was heuristically established and applied to the NCC ToF estimations for all transmitter-receiver pairs and reconstructions. To avoid using echo information, the NCC maximum search was restricted to a time window around the first arrival time based on the *a priori* SoS, with a margin of ± 0.15 times the estimated travel time for each transmitter-receiver pair.

For the experimental data, post-processing isolated the first arrival and significantly reduced noise. As a result, a simplified Balda-based algorithm [43], [44] was used to identify the onset of the first arrival and estimate the ToF. The parameters of the Balda algorithm were set to their standard values [44]. Similar to the approach used for the simulation data, to minimize the impact of spurious data, ToF estimations were considered valid for each transmitter-receiver pair only if they fell within an interval of ± 0.10 times the standard deviation of all estimated travel times for the same transmitter.

As described in Section II-A, the forward problem must be estimated in order to solve the reconstruction inverse problem. For that, a Multi-Stencil High Accuracy Fast Marching Method (MSHAFMM) with eight neighbors was implemented based on [23] and [45]. The ray-paths were determined by back-propagating a descent gradient over the MSHAFMM-computed time delay maps, initiating from each receiver for every transmitter. For solving (12), the steepest descent method with Total Variation L^1 [31] regularization was conducted. To enhance stability and ensure convergence a modified Barzilai-Borwein method [46], [47] was preferred over the traditional approach [48] for calculating the step size in each descent iteration. As the main goal of this work is not to investigate the best reconstruction parameters, the regularization parameters were determined heuristically. All codes were implemented in MATLAB 2020b, except for the MSHAFMM, which was implemented in C++ with a MEX interface for the computational efficiency. No parallelization was performed. For solving the boundary optimization problem, a straightforward approach

using the *mldivide* (\) MATLAB 2020b built-in function was applied to the Moore-Penrose pseudo-inverse as outlined in (29). This method proved to be both rapid and robust for the matrix conditions, as evidenced by the results discussed in Section IV. All reconstructions were conducted on a Thinkpad L14 Gen1 Laptop, equipped with a Ryzen 7 Pro 4750 1700 MHz CPU, no dedicated GPU, and 32 GB of RAM. Henceforth, the reconstruction method without expected gradient and boundary optimization is referred to as the standard method.

IV. Results and Discussion

A. Numerical Simulation Results and Discussion

The *in silico* data reconstructions were computed on a square discretized grid of 151×151 pixels. As previously mentioned, the regularization parameters were determined heuristically. To ensure unbiased results across the different abnormal phantoms, the parameters were first set using the reference phantom for each method (standard or proposed) and then used for all pathological cases. The regularization parameter for speed of sound optimization was set to $\alpha_1 = 1 \times 10^{-4}$ for the standard method and $\alpha_1 = 1 \times 10^{-8}$ for the proposed method. For boundary optimization, the parameter was set to $\alpha_2 = 0.05$. Additionally, the total variation L^1 norm approximation constant for large-scale problems was set to $\beta = 5 \times 10^{-7}$ for the standard method and $\beta = 7.5 \times 10^{-13}$ for the proposed method.

The global stopping criterion involved five forward problem updates. For the steepest descent algorithm, the algorithm stopped after a maximum of 100 iterations or a dual-condition criterion requiring a relative residual error (RRE) smaller than 1×10^{-10} and a derivative less than 1×10^{-14} in absolute value to ensure minimal change in the RRE. The *a priori* speed of sound was set to 1540 m/s in both the domain and its boundary, following the standard convention for the average body speed of sound in the ultrasound field [49].

The quantitative metrics used for evaluating the proposed method *in silico* were the Root Mean Square Error (RMSE) and Universal Quality Index (Q) [50], defined as following for discrete (x, y) positions

$$RMSE = \sqrt{\frac{\sum_{x=1}^{Nx}\sum_{y=1}^{Ny}(R(x,y) - G(x,y))^2}{NxNy}} \tag{30}$$

$$Q = \left(\frac{\sigma_{GR}}{\sigma_R \sigma_G}\right)\left(\frac{2\mu_G\mu_R + sc}{{\mu_G}^2 + {\mu_R}^2 + sc}\right)\left(\frac{2\sigma_R\sigma_G + sc}{{\sigma_R}^2 + {\sigma_G}^2 + sc}\right) \tag{31}$$

where, G, R, μ, σ and σ_{GR} are the gold standard image, the reconstruction image, the mean, standard deviation and images covariance, respectively. The sc parameter is a stabilizing coefficient defined as

$$sc = \frac{(\max(G(x,y)) - \min(G(x,y)))^2}{1000}. \tag{32}$$

Also, the root mean square error (RMSE) was calculated between the perturbed sensor positions and the ground truth, following a definition similar to (30), as the metric for the sensor positioning optimization.

To assess the optimization of sensor positions, normally distributed perturbations were introduced along the normal direction with zero mean and standard deviations of 0 mm (no perturbation), 5 mm (low perturbation), 10 mm (medium perturbation), and 15 mm (high perturbation). These imprecision levels simulate the measurement and basal activity-induced errors in a reasonable way. In practical applications, boundary errors typically affect sensor clusters rather than isolated units. Therefore, these perturbations were smoothed by averaging the disturbances from the six nearest neighboring sensors. To evaluate the impact of this smoothing process, 1000 random perturbations were generated for each perturbation level. Prior to smoothing, the average standard deviations corresponded to the specified values, and the L^∞ norm positioning errors were 13.03 mm for the low perturbation, 26.21 mm for the medium perturbation, and 39.06 mm for the high perturbation. The smoothing process resulted in an average reduction of 64.56% in standard deviation and 66.14% in L^∞ norm positioning error for all perturbation levels. Consequently, the post-smoothing average L^∞ norm positioning errors were 4.39 mm, 8.95 mm, and 13.18 mm for the low, medium, and high perturbation levels, respectively. Despite the substantial reductions, the smoothed perturbations provides a more realistic condition, accounting for belt tension.

Reconstructions for all phantoms, under low and high perturbations, using the standard and proposed methods, can be seen in Figs. 6 and 7, respectively. The red scattered dots represent the imprecise sensor center positions resulting from the perturbation noise addition, while the updated center positions, after applying the boundary optimization algorithm, are shown as black scattered dots. As the displacements are assumed to be in the normal direction, the positions were represented by the center of the transducer without loss representation. The qualitative evaluation of the aforementioned figures shows a clear improvement, especially for high perturbation scenarios, as the original boundary shape defined by the transducers almost perfectly recovered. This suggests that the method is capable of accurately retrieving the sensor positions in a fully *a posteriori* approach.

The organs boundaries and details are better retrieved, and the outer boundary is exceptionally well recovered. Also, the small pathologies in phantom 2 are better visualized with the proposed method. Notably, the new method achieves convergence in the reconstructions with a smaller regularization factor, improving the quality of details, as evidenced by the universal quality index comparison for all phantoms with some kind of boundary perturbation included. Additionally, this less regularized scenario is crucial for maintaining the physical realism of the reconstruction without altering its morphology and values to achieve convergence. It is also noteworthy that high speed regions are observed in the edema areas. These regions are particularly evident in the reconstructions shown in Fig. 6(c), (d), (e), and (f). This phenomenon arises due to an averaging effect inherent to the solution method, which is influenced by the higher SoS in the bones and edemas. Interestingly, these high-speed regions outline the inner contours of the edemas, a feature that could potentially assist in diagnosing abnormalities.

TABLE II
QUANTITATIVE COMPARISON BETWEEN THE RESULTS WITH NONE, LOW, MEDIUM AND HIGH PERTURBATIONS USING THE STANDARD METHOD AND THE PROPOSED METHOD

Perturbation	Metric	Reference Phantom		Phantom 1		Phantom 2	
		Standard method	Proposed method	Standard method	Proposed method	Standard method	Proposed method
–	RMSE $[m/s]$	66.2113	66.6475	67.5841	66.5592	66.5236	66.7106
	Q	0.6376	0.6471	0.6026	0.6115	0.6138	0.6214
Low	RMSE $[m/s]$	63.7468	64.4886	67.2013	65.9134	73.8556	70.8084
	Q	0.6268	0.6329	0.5883	0.6061	0.5984	0.6241
Medium	RMSE $[m/s]$	70.0939	66.6010	67.8822	64.0928	67.2093	65.9181
	Q	0.5810	0.6319	0.5602	0.5909	0.5767	0.6065
High	RMSE $[m/s]$	76.5827	70.7576	79.3121	66.7949	67.5608	65.3951
	Q	0.5692	0.6342	0.5316	0.5854	0.5750	0.5947

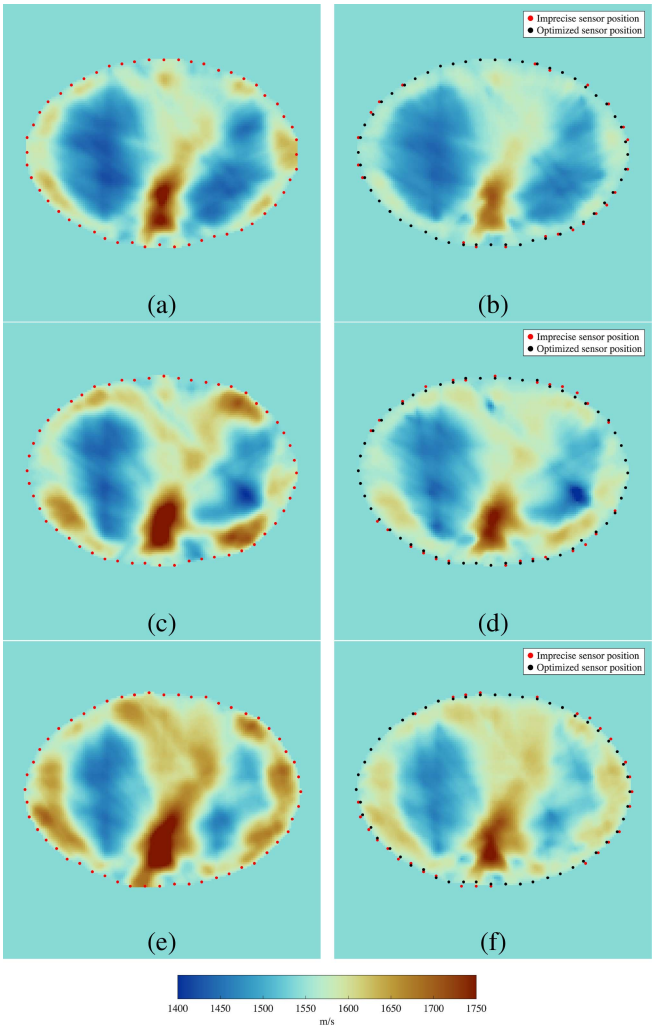

Fig. 6. Reference phantom, phantom 1, and phantom 2 reconstructions with the low perturbation in sensor positions using the standard method (a), (c), (e) and the proposed method (b), (d), (f). The red scattered dots represent the imprecise sensor positions and the black ones the optimized.

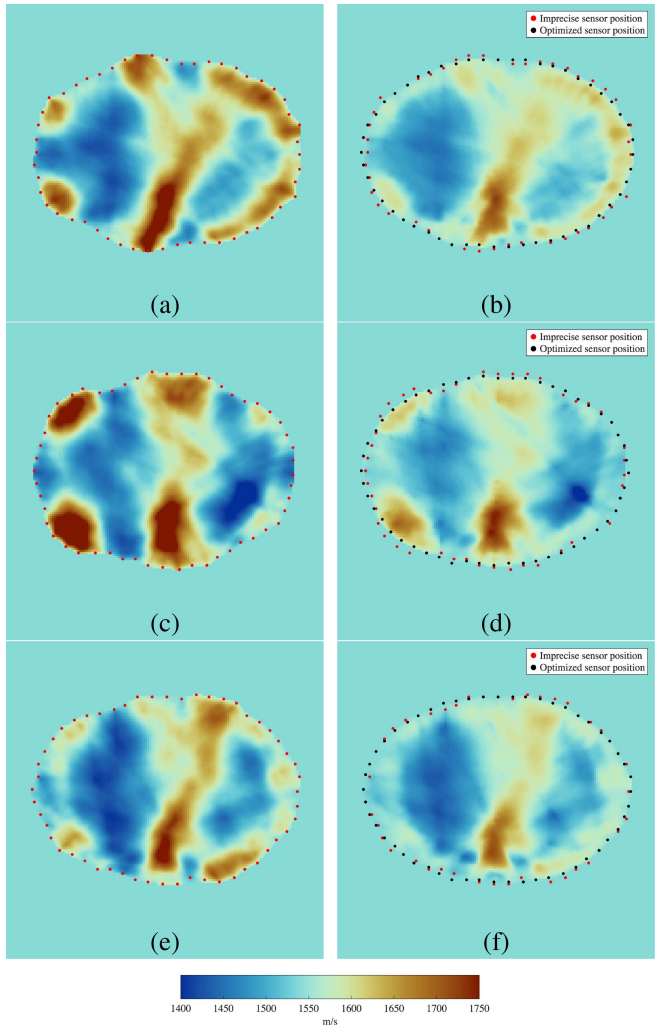

Fig. 7. Reference phantom, phantom 1, and phantom 2 reconstructions with the high perturbation in sensor positions using the standard method (a), (c), (e) and the proposed method (b), (d), (f). The red scattered dots represent the imprecise sensor positions and the black ones the optimized.

The sensor position RMSE improvement is shown in Table III for all phantoms and perturbation levels. Quantitative results for the reconstructions and their respective perturbation levels are presented in Table II. The effects of the expected gradient without the sensor positioning optimization can be seen in the results with no position perturbation. These were computed without the sensor correction algorithm part. It is observed that the proposed method produces slightly better or similar results to the standard method in the no-perturbation scenario. However, when perturbations were added, the proposed method consistently outperforms the standard method across all metrics. Additionally, the optimized sensor positioning reduces the position RMSE in every perturbed scenario as can be seen in

TABLE III
SENSOR POSITIONING RMSE FOR THE EVALUATION OF SENSOR POSITIONS RETRIEVAL

	Perturbation	Sensor positioning RMSE $[mm]$ Before optimization	After optimization
Reference Phantom	Low	1.4215	1.5376
	Medium	2.3070	1.0478
	High	3.2538	1.3455
Phantom 1	Low	1.097	1.0289
	Medium	2.5528	1.6951
	High	3.8940	1.6810
Phantom 2	Low	1.5432	0.8523
	Medium	2.1683	1.3843
	High	3.1516	2.1219

Table III. The similar performance of the methods in scenarios with no or minimal perturbations may be due to numerical approximations and discretization imprecision, as the sensor positioning optimization relies on the sensor grid positioning when executing the forward problem approximation.

B. Experimental Data Results and Discussion

After demonstrating the feasibility of the proposed method through numerical results, we validated its robustness in a real-world scenario using rf-US signals acquired with a ballistic gel phantom. The *ex vivo* experimental data reconstruction was performed on a square grid of 71×71 pixels. This grid is coarser than the numerical data reconstruction grid to reduce the problem's ill-conditioning and underdetermination by using fewer pixels. This adjustment is necessary due to the reduced amount of information from the 28 transducers compared to the 52, and is feasible given the simpler geometry of the ballistic gel phantom.

The regularization parameter for speed of sound optimization was set to $\alpha_1 = 5 \times 10^{-5}$, while the parameter for boundary optimization was set to $\alpha_2 = 0.05$. Additionally, the total variation L_1 norm approximation constant for large-scale problems [31] was set to $\beta = 1 \times 10^{-7}$ for the standard method and $\beta = 1 \times 10^{-11}$ for the proposed method. The same global and steepest gradient stopping criteria from the *in silico* reconstructions were applied to the experimental data reconstruction. Given the higher average speed of sound in ballistic gel compared to water, the *a priori* conjectured speed of sound was set to 1700 m/s in both the domain and its boundary.

Two different setup scenarios were presented for the phantom and its cavities. The first scenario involved the phantom with empty cavities containing only air, simulating high contrast in speed of sound and attenuation. The second scenario involved the phantom with cavities filled with water and a cylindrical plastic container with air, negligible walls, and a 33.9 mm radius, immersed in the center of the right cavity. This setup aimed to evaluate the method precision regarding smaller structures in a complex environment with three different speed of sound regions (ballistic gel, water, and air).

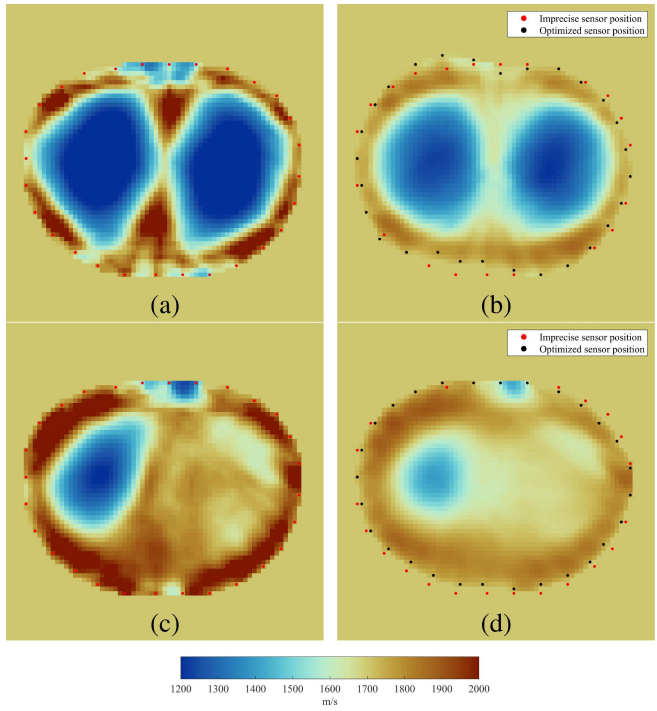

Fig. 8. Reconstruction of the ballistic gel torso with empty cavities reconstruction using the standard method (a) and the proposed method (b). Reconstruction of the ballistic gel torso with the left cavity filled with water, and right cavity also filled with water and a empty plastic bottle immersed in in it using the standard method (c) and the proposed method (d). The red scattered dots represents the imprecise sensor positions and the black ones the optimized.

Since no ground truth was available for the ballistic gel phantom reconstruction, the evaluation was primarily qualitative. The only quantitative metric used was the transverse cross-sectional area of the cavities and the plastic container. The cavities and plastic container were segmented using a threshold segmentation approach. To estimate the areas containing only air, pixels with a speed of sound below 1500 m/s were classified as air regions. Hence, areas were computed by multiplying the number of thresholded pixels by the pixel area. The expected values for transverse cross-sectional area of the cavities and the plastic container are respectively $1.9007 \times 10^{-2}\,\mathrm{m}^2$ and $3.6104 \times 10^{-3}\,\mathrm{m}^2$.

Qualitative results using both methods for the empty cavities setup are shown in Fig. 8(a) and (b), while those for the the plastic container setup are shown in Fig. 8(c) and (d). The proposed method clearly provided better geometry retrieval for both the cavity and the plastic container. The relative error ($E_{\%}$) between the actual transverse cross-sectional area of air regions (A_{actual}) and the estimated values (A_{estim}) was used as a quantitative evaluation metric. It was calculated as

$$E_{\%} = \frac{A_{actual} - A_{estim}}{A_{actual}} \cdot 100. \tag{33}$$

The quantitative results of the air regions, presented in Table IV, support the qualitative evaluation. The standard method tends to overestimate areas of higher contrast, which would definitely hinder clinical lung imaging.

TABLE IV
RELATIVE ERROR OF THE AIR REGION AREA

	Air region area relative error [%]	
Setup	Standard method	Proposed method
Empty cavities	48.6137	2.5727
Plastic container	88.4445	−33.7193

One can observe in Fig. 8, a small low speed of sound region in the phantom posterior. Although this might appear to be an artifact, it is actually due to the phantom posterior dip filled with ultrasound coupling gel, which has a lower speed of sound compared to ballistic gel. Before acquiring this experimental setup, the region was completely filled with gel to ensure a better fit for the transducer belt. In a qualitative evaluation, it is notable that the proposed method was able to better handle the dip geometry and the positioning imprecision than the standard method.

Furthermore, high SoS contrast reconstruction remains a challenge in quantitative TFTM USCT. As a result, the reconstructed SoS value for air does not match the expected 340 m/s. In Fig. 8(d), the air region shows a lower SoS than in Fig. 8(b), which is due to the size of the air region. Larger heterogeneous structures contribute more information to the reconstruction system, influencing the gradient step direction. Since the air region is smaller in Fig. 8(d), the gradient step towards a lower SoS is less pronounced in the optimization method, reducing contrast. Additionally, smaller structures are more affected by smoothing due to regularization.

It is also noteworthy that the experimental data reconstruction used fewer transducers but had a less intricate inner structure than the numerical simulated data. Future work should evaluate the impact of a more complex inner structure with few transducers. Nonetheless, the results demonstrate greater robustness with the proposed method, indicating it is the right approach for future studies.

V. CONCLUSION

This work presents a method to improve the quality and robustness of time of flight transmission mode ultrasound tomography (TFTM USCT) encompassing two key improvements. A new approach for calculating the step in each steepest descent iteration was proposed by using an expected value for the gradient. The motivation for this new approach was the concentration of information and high penalization of specific pixels (especially near transducers) during the reconstruction procedure. Also, as the patient presents a basal movement, and measurements are always imprecise, there is uncertainty in the assumed transducers locations. Since TFTM USCT is completely based on positions and delays, and bedside imaging relies in non-rigid hardware, the results are severely compromised by this type of error. Therefore, along with the expected gradient, an *a posteriori* sensor positioning optimization method is proposed in order to address this issue. The results demonstrate that the proposed method outperforms the standard method for TFTM USCT in every metric used for all of the presented numerically simulated perturbed scenarios and experimental data. Moreover, the proposed method was capable of retrieving the morphology of the known sensor distribution of numerically simulated data. Future work shall comprise the exploration of the sensor positioning error character and how it affects imaging in other scenarios.

ACKNOWLEDGMENT

The content is solely the responsibility of the authors and does not necessarily represent the official views of the National Institutes of Health. The Scientific colour map used in this study was developed by Crameri et al. [DOI: 10.1038/s41467-020-19160-7].

REFERENCES

[1] F. Crameri, G. E. Shephard, and P. J. Heron, "The misuse of colour in science communication," *Nature Commun.*, vol. 11, 12 2020, Art. no. 5444.
[2] R. J. Lavarello and A. J. Hesford, *Methods for Forward and Inverse Scattering in Ultrasound Tomography*. Dordrecht, Netherlands: Springer Netherlands, 2013, pp. 345–394.
[3] D. M. Technologies, "The SoftVue system," 2024, Accessed: Dec. 7, 2025. [Online]. Available: https://www.delphinusmt.com/softvue/
[4] A. Sustic, "Role of ultrasound in the airway management of critically ill patients," *Crit. Care Med.*, vol. 35, pp. S173–S177, 2007.
[5] C. L. Tobin et al., *Pleural Ultrasound for Clinicians: A Text and E-Book*. Boca Raton, FL, USA: CRC Press, 2014.
[6] D. Rueter et al., "Low-frequency ultrasound permeates the human thorax and lung: A novel approach to non-invasive monitoring," *Ultraschall der Medizin - Eur. J. Ultrasound*, vol. 31, pp. 53–62, 2009.
[7] K. Morenz et al., "Detection of air trapping in chronic obstructive pulmonary disease by low frequency ultrasound," *BMC Pulmonary Med.*, vol. 12, pp. 8–8, 2012. [Online]. Available: https://api.semanticscholar.org/CorpusID:6607707
[8] A. V. Pigatto et al., "Luft: A low-frequency ultrasound tomography system designed for lung imaging," *IEEE Sensors J.*, vol. 24, pp. 11091–11101, 2024. [Online]. Available: https://ieeexplore.ieee.org/document/10430118/
[9] A. V. Pigatto et al., "Design and calibration of a tonpilz transducer for low frequency medical ultrasound tomography," in *Proc. 2022 44th Annu. Int. Conf. IEEE Eng. Med. Biol. Soc.*, 2022, pp. 4611–4617.
[10] R. Lavarello and M. Pelze, "A study on the reconstruction of moderate contrast targets using the distorted born iterative method," *IEEE Trans. Ultrason., Ferroelectr., Freq. Control*, vol. 55, no. 1, pp. 112–124, Jan. 2008.
[11] K. Wang et al., "Waveform inversion with source encoding for breast sound speed reconstruction in ultrasound computed tomography," *IEEE Trans. Ultrason., Ferroelectr., Freq. Control*, vol. 62, no. 3, pp. 475–493, Mar. 2015.
[12] J. Rao et al., "Multi-parameter reconstruction of velocity and density using ultrasonic tomography based on full waveform inversion," *Ultrasonics*, vol. 101, 2020, Art. no. 106004.
[13] M. S. Manuchehri and S. K. Setarehdan, "A robust time delay estimation method for ultrasonic echo signals and elastography," *Comput. Biol. Med.*, vol. 136, 2021, Art. no. 104653.
[14] M. Jaëger et al., "Full correction for spatially distributed speed-of-sound in echo ultrasound based on measuring aberration delays via transmit beam steering," *Phys. Med. Biol.*, vol. 60, pp. 4497–4515, 2015.
[15] P. Stähli et al., "Improved forward model for quantitative pulse-echo speed-of-sound imaging," *Ultrasonics*, vol. 108, 2020, Art. no. 106168.
[16] R. Rau et al., "Speed-of-sound imaging using diverging waves," *Int. J. Comput. Assist. Radiol. Surg.*, vol. 16, pp. 1201–1211, 2021.
[17] A. Hormati et al., "Robust Ultrasound travel-time tomography using the bent ray model," *Proc. SPIE*, vol. 7629, 2010, Art. no. 76290I.
[18] R. Ali, S. Hsieh, and J. Dahl, "Open-source Gauss-Newton-based methods for refraction-corrected ultrasound computed tomography," *Proc. SPIE*, vol. 10955, pp. 39–52, 2019.
[19] L. E. Kinsler et al., *Fundamentals of Acoustic*, 4th ed. Hoboken, NJ, USA: Wiley, 2000.
[20] B. E. Treeby and B. T. Cox, "k-wave: Matlab toolbox for the simulation and reconstruction of photoacoustic wave fields," *J. Biomed. Opt.*, vol. 15, no. 2, 2010, Art. no. 021314.

[21] S. F. Potter, M. K. Cameron, and R. Duraiswami, "Numerical geometric acoustics: An Eikonal-based approach for modeling sound propagation in 3 d environments," *J. Comput. Phys.*, vol. 486, 2023, Art. no. 112111.
[22] J. Sethian, *Level Set Methods and Fast Marching Methods*, 2nd ed. Cambridge, U.K.: Cambridge Univ. Press, 1999.
[23] M. S. Hassouna and A. A. Farag, "Multistencils fast marching methods: A highly accurate solution to the Eikonal equation on Cartesian domains," *IEEE Trans. Pattern Anal. Mach. Intell.*, vol. 29, no. 9, pp. 1563–1574, Sep. 2007.
[24] C. Li and M. J. King, "Impact of heterogeneity upon the accuracy of the Eikonal solution using the fast marching method," *Comput. Geosciences*, vol. 27, pp. 465–484, 2023, doi: 10.1007/s10596-023-10204-7.
[25] G. T. Schuster, *Seismic Inversion*, 1st ed. Society of Exploration Geophysicists, 2017, vol. 1.
[26] A. N. Tikhonov et al., *Numerical Methods for the Solution of Ill-Posed Problems*, 1st ed. Netherlands: Springer, 1995.
[27] A. Javaherian, F. Lucka, and B. T. Cox, "Refraction-corrected ray-based inversion for three-dimensional ultrasound tomography of the breast," *Inverse Problems*, vol. 36, 2020, Art. no. 125010.
[28] A. Björck, *Numerical Methods for Least Squares Problems*, 1st ed., Philadelphia, PA, USA: Society for Industrial and Applied Mathematics, 1996.
[29] C. Li et al., "In vivo breast sound-speed imaging with ultrasound tomography," *Ultrasound Med. Biol.*, vol. 35, pp. 1615–1628, 2009.
[30] M. Alsaker et al., "Complementary use of priors for pulmonary imaging with electrical impedance and ultrasound computed tomography," *J. Comput. Appl. Math.*, vol. 395, 2021, Art. no. 113591.
[31] J. L. Mueller and S. Siltanen, *Linear and Nonlinear Inverse Problems With Practical Applications*, 1st ed. Philadelphia, PA, USA: SIAM, 2012. [Online]. Available: https://epubs.siam.org/doi/abs/10.1137/1.9781611972344
[32] R. C. Aster, B. Borchers, and C. H. Thurber, *Parameter Estimation and Inverse Problems*, 3rd ed. New York, NY, USA: Elsevier, 2019.
[33] B. Bergman, A. Tryggvason, and C. Juhlin, "Seismic tomography studies of cover thickness and near-surface bedrock velocities," *Geophysics*, vol. 71, pp. U77–U84, 2006.
[34] A. Tryggvason, C. Schmelzbach, and C. Juhlin, "Traveltime tomographic inversion with simultaneous static corrections — well worth the effort," *Geophysics*, vol. 74, pp. WCB25–WCB33, 2009.
[35] J. B. Rosen et al., "Accurate solution to overdetermined linear equations with errors using l1 norm minimization," *Comput. Optim. Appl.*, vol. 17, pp. 329–341, 2000.
[36] J. Baumeister and A. Leitão, *Topics in Inverse Problems*, 1st ed. Rio de Janeiro, Brazil: IMPA Mathematical Publications, 2005.
[37] L. Oneto, S. Ridella, and D. Anguita, "Tikhonov, Ivanov and Morozov regularization for support vector machine learning," *Mach. Learn.*, vol. 103, pp. 103–136, 2016.
[38] F. S. Lobato and V. Steffen, *Multi-Objective Optimization Problems*. Berlin, Germany: Springer, 2017, doi: 10.1007/978-3-319-58565-9.
[39] B. E. Treeby et al., "Modeling nonlinear ultrasound propagation in heterogeneous media with power law absorption using a K-space pseudospectral method," *J. Acoust. Soc. Amer.*, vol. 131, pp. 4324–4336, 2012.
[40] J. L. Mueller et al., "Estimating regions of air trapping from electrical impedance tomography data," *Physiol. Meas.*, vol. 39, 2018, Art. no. 05NT01.
[41] R. Levin, C. M. Bono, and S. R. Garfin, *Vertebral Discitis and Osteomyelitis*. Amsterdam, The Netherlands: Elsevier, 2005, pp. 212–225.
[42] T. D. White, M. T. Black, and P. A. Folkens, *Hyoid and Vertebrae*. Amsterdam, The Netherlands: Elsevier, 2012, pp. 129–147.
[43] R. Balda et al., "The HP ECG analysis program," in *Trends in Computer Processed Electrocardiograms*, Amsterdam, Netherlands: North Holland, 1977, pp. 197–205.
[44] M. Elgendi et al., "Revisiting QRS detection methodologies for portable, wearable, battery-operated, and wireless ecg systems," *PLoS One*, vol. 9, 2014, Art. no. e84018.
[45] S. Merino-Caviedes et al., "A second order multi-stencil fast marching method with a non-constant local cost model," *IEEE Trans. Image Process.*, vol. 28, no. 4, pp. 1967–1979, Apr. 2019.
[46] S. Yang and S. L. Wu, "A modified Barzilai-Borwein algorithm for the generalized absolute value equation," *Operations Res. Lett.*, vol. 51, pp. 21–25, 2023.
[47] H. Jalilian, "Total variation method based on modified Barzilai–Borwein algorithm to noise reduction in MRI images," *J. Supercomputing*, vol. 80, pp. 601–619, 2024.
[48] J. Barzilai and J. M. Borwein, "Two-point step size gradient methods," *IMA J. Numer. Anal.*, vol. 8, pp. 141–148, 1988.
[49] T. L. Szabo, *Diagnostic Ultrasound Imaging: Inside Out*, 2nd ed. New York, NY, USA: Elsevier, 2004.
[50] Z. Wang and A. C. Bovik, "A universal image quality index," *IEEE Signal Process. Lett.*, vol. 9, no. 3, pp. 81–84, Mar. 2002.